Numerical simulation and evaluation of Y_2S_3 and Y_2TeS_2 on structural, stability, and electronic properties for photocatalytic water splitting applications

Original Research Article

Abstract

We attempt to establish a computational insight into the structural, mechanical, dynamic, electronic, and photocatalytic properties of orthorhombic phase Yttrium sulphide Y_2S_3 and Y_2TeS_2 Janus compounds by density functional calculations. The Janus Y_2TeS_2 is a hypothetical compound with all properties computed for the first time. Computed lattice parameters for Y_2S_3 are in reasonable agreement with available experimental data. Mechanical properties are investigated by calculating the elastic constant to check for Born stability criteria. A finite displacement vibrational frequency study confirmed that Y_2S_3 and Y_2TeS_2 are stable; negative phonon frequencies were checked. Computed PBEsol and MBJ band structures found that Y_2S_3 is a direct band gap semiconductor, while Y_2TeS_2 is an indirect band gap semiconductor. Band gaps estimated from the HSE06 hybrid functional are 2.75 eV and 2.70 eV for Y_2S_2 and Y_2TeS_2, respectively, suggesting that they are semiconductor materials with wide band gaps that can absorb light in the ultraviolet region. Mullikan's electronegativity screen technique, used to calculate valence band maximum VBM and conduction band minimum CBM potentials, predicted that Y_2S_3 and Y_2TeS_2 have suitable conduction band minimum potential of -1.05 V and -1.30 V and valence band maximum of 1.70 V and 1.40 V, respectively, versus normal hydrogen electrode (NHE) at PH = 0 to trigger the oxygen evolution reaction (OER) and hydrogen evolution reaction (HER) simultaneously.

Keywords: Rare-earth; Chalcogenide; Photocatalytic; DFT

1 Introduction

Rare-earth-containing chalcogenide elements are particularly interesting because of their diverse structural chemistry and physical properties. The rare earth is related to the chemistry of 4f electrons; possession of 4f orbital

---

occupancy has a significant function of electronic modulation that enhances the electronic and optical properties of materials (1). Rare earths are dopants in transition metal oxides and transition metal chalcogenides. They were widely explored and reported to enhance their application in photocatalysis and thermoelectric, including optoelectronic materials. Rare-earth doped metal oxides have been reported to modify photocatalytic properties effectively (2; 3) and materials band gap turning (4), pollutant degradation (5; 6). Recent research conducted on rare-earth metal-doped metal chalcogenides has further confirmed the capability of rare earth metal to enhance the electronic and optical properties (7); others are photocatalytic properties (8; 9). In the area of photocatalytic applications, early and recent research has shown that rare-earth metal chalcogenides demonstrate the potential of a future promising photocatalytic material. This was confirmed from previous research, such as the magnetic and photocatalytic properties of $\mathrm{Dy_4S_4Te_3}$ (10), physical and photocatalytic properties of $\mathrm{RE_4S_4Te_3}$ (RE = Gd, Ho, Er, and Tm) (11), others are the photocatalytic activity of GeSbSeEr (12), photoluminescence and photocatalytic properties of α-$\mathrm{EuZrS_3}$ (13), and electronic and optical properties are reported in $\mathrm{Y_2MgX_4}$ (X = S, Se, and Te) (14) and YX (X = S, Se, and Te) (15). Rare-earth sulphides are among the most researched rare-earth materials, owing to their tunable wide band gap. The Rare-earth sulfide possesses various applications, including the electrolyte materials, thermoelectric (16), optical material (17), and supercapacitors (18). Among the rare-earth sulfides, yttrium sulfide $\mathrm{Y_2S_3}$ received attention for applications such as pressure-dependent optical properties (19), thermoelectric material (20), and electrolyte material (21). Three crystal phases of yttrium sulfide $\mathrm{Y_2S_3}$ were known, the cubic, monoclinic, and orthorhombic phases (19; 21; 22). Because of the role played by rare-earth material and its doping capabilities in improving other material properties, such as photocatalytic efficiency, physicochemical, electronic, and optical, and in particular the tunable wide band gap possessed by $\mathrm{Y_2S_3}$. The excellent tunable band gap property of $\mathrm{Y_2S_3}$ can be useful for photocatalytic properties studies. In this study, we investigate using state-of-the-art density functional theory the physical properties and photocatalytic application of orthorhombic phase yttrium sulphide $\mathrm{Y_2S_3}$. The $\mathrm{Y_2S_3}$ was found to be stable under high-pressure phase transition (19). Another compound is the yttrium sulphide tellurite $\mathrm{Y_2TeS_2}$ Janus-structured materials. The $\mathrm{Y_2TeS_2}$ was investigated for the first time; the structure is derived from the material-project software (23). Recently, a similar compound, yttrium sulphide selenide (YSSe), a Janus two-dimensional material, was predicted by (24) using first principle calculations.

2 Computational Method

In this work the calculations were carried out based on density functional theory (DFT) (25; 26) implemented in the Vienna $ab\ initio$ simulation package (VASP) (27). VASP expands the pseudopotential part of Kohn-Sham one-electron spin orbitals $\psi_i^{\sigma,\mathbf{k}}(\mathbf{r})$ on a basis set of plane waves to solve the self-consistent Kohn-Sham (KS) Schr$\ddot{o}$dinger-like eigen equation (25).

$$\left\{-\frac{\hbar^2}{2m_e}\nabla_i^2+\int\frac{n(\mathbf{r}')}{|\mathbf{r}-\mathbf{r}\prime|}+V_{ext}(\mathbf{r})+V_{XC}^{\sigma,\mathbf{k}}[n(\mathbf{r})]\right\}\psi_i^{\sigma,\mathbf{k}}(\mathbf{r})=\epsilon_i^{\sigma,\mathbf{k}}\psi_i^{\sigma,\mathbf{k}}(\mathbf{r}) \tag{2.1}$$

Kohn-Sham DFT is the robust method employed for ground state electronic structure calculation of materials and molecules. For this calculation, the Perdew-Burke-Ernzehof generalized gradient approximation revised for solids and their surfaces (PBEsol) functional was employed for computational studies. It was reported to predict the mechanical stability of metal chalcogenide material semiconductor (28), and a plane wave basis with projected augmented wave (PAW) potential (29) was chosen to treat the exchange energy correlation effect. For decades, the PAW basis set framework has offered remarkable efficiency and accuracy to Kohn-Sham DFT calculations for molecules and extended solids. For equilibrium structure optimization, we used the primitive cell structure of $\mathrm{Y_2S_3}$ and $\mathrm{Y_2TeS_2}$ with the choice of plane-wave with kinetic energy. $-\frac{\hbar^2}{2m_e}|\mathbf{k}-\mathbf{G}|<E_{cut}$ of 520 eV. The k-point sampling integral over the irreducible Brillouin zones is performed up to 8×3×3 and 6×8×10 for $\mathrm{Y_2S_4}$ and $\mathrm{Y_2TeS_2}$, respectively, using the Monkhorst-Pack mesh (30) approach that was chosen to achieve convergence energies within less than 1 meV/atom. From the optimized structure, the elastic tensor and phonon dispersion were calculated.

Phonon calculation was performed using the finite displacement supercell technique as implemented in the phonopy package (31). In the finite displacement method, one or multiple atoms are displaced, and forces on atoms are calculated from the force constant equation: (32; 33)

$$f_{lk\alpha}=\sum_{l'k'\alpha'}\phi_{|k\alpha,l'k'\alpha'|}U_{l'k'\alpha'} \tag{2.2}$$

From the Brillouin zone integration calculation, the phonon density of state (DOS) per unit cell was determined from the equation,$D(\omega)=\frac{1}{N}\sum_{\mathbf{q}v}\delta(\omega-\omega_{\mathbf{q}v})$ and the projected contribution of atom to DOS from $D_{k\alpha}(\omega)=$

$\frac{1}{N}\sum_{\mathbf{qk}}\delta(\omega-\omega_{\mathbf{qk}})|\mathbf{W}_{\mathbf{q}\alpha}(\mathbf{qk})$. The vibrational frequency $\omega_{\mathbf{qk}}$ is the product of the square root of the eigenvalues of the dynamical equation:

$$D_{s\alpha,t\beta}(\mathbf{q}) = \frac{\mathbf{1}}{\sqrt{\mathbf{M_s M_t}}}\sum_{\mathbf{l}}\phi_{\mathbf{ls}\alpha,\mathbf{0t}\beta}\mathbf{exp}[\mathbf{iq}.(\mathbf{R_0}+\tau_{\mathbf{t}}-\mathbf{R_l}-\tau_{\mathbf{s}})] \tag{2.3}$$

where $R_0+\tau_t$ represents the equilibrium position with atom s of mass M_s in primitive cell l, the sum runs over the infinite number of primitive cells in the crystal. With the known force constant equation 2.2, the dynamic matrix $D_{s\alpha,t\beta}$ and frequency ω_{qk} were obtained at any $\mathbf{q}$.

Electronic structure calculation, including band structure and density of state based on GGA-PBEsol, hybrid functional, the modified Becker Johnson potential (mBJ) (34) and Heyd-Scuseria-Ernzerhof (HSE)(35) within the DFT, was performed. The PBEsol/HSE exchange-correlation functional was also used for the calculation of the dielectric constant for the determination of optical properties. HSE and MBJ functional were reported to successfully describe properties of bulk semiconducting and insulating condensed systems. The HSE functional treats the electron-electron interaction partly with long-range 75% semi-local PBE-xc functional and 25% short-range non-local Hartree-Fock exchange.

3 Result and Discussion

Structural properties

The relaxed crystal structure of Y_2S_3 and Y_2TeS_2 is viewed in the b-a axis in Figure 1; both compounds are orthorhombic crystals. Y_2S_3 was experimentally observed with space group Pnnm (19) under unreversible pressure transition (19). The result of the structural optimization, the lattice parameters, and the optimized volume of Y_2S_3 and Y_2TeS_2 are seen in Table 1. Depending on the combination of the metal and chalcogenide (S, Se, and Te) elements, the physical properties such as structural, mechanical, dynamic, and electronic properties are modified (36; 37). The lattice parameter compared to experimentally derived values shows an increase of $<$ 0.6%. This is expected of the PBEsol accurate prediction of structural properties. The substitution of tellurium in Y_2S_3 structure significantly regulates the crystal lattice parameters and volume the percentage deviation is recorded in Table 1. The calculation of structural optimization for Y_2TeS_2 shows an increase of $<$ 30% of lattice parameter a, $b/$, and a decrease of $<$ 50% for lattice parameter c and volume V compared to that of Y_2S_3 material. This structural change is reflected in the calculated elastic constant (c$_{ij}$) and its derived parameter values (Bulk, Young, Shear modulus) as observed in Table 2 and 3. .

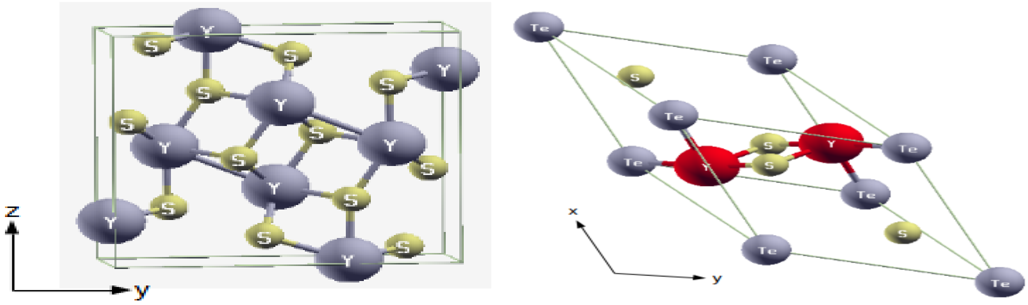

Figure 1: The unit cell structure of Y_2S_3 right z - y direction and Y_2TeS_2 left in x - y direction side view respectively.

Mechanical stability

First-principles calculation was widely accepted for studies of mechanical and phonon stabilities of semiconductor materials. Mechanical properties were linked to elastic constant, which gives insight into material characteristics

Table 1: Calculated values of lattice parameters, crystal angles; α, β, γ in degree and optimized volume for Y_2S_3, Y_2TeS_2 and the percentage deviation from experimental values(22; 19) and the deviation of Y_2TeS_2 values from that of Y_2S_3 structure with PBEsol functional

	a (Å)	b (Å)	c (Å)	α	β	γ	V (Å^3)
Y_2S_3	10.65 (+0.43%)	3.87(+0.38%)	10.49(+0.56%)	90	90	90	432.79
Y_2TeS_2	13.48(+26.57%)	4.19(+8.27%)	5.35(-49%)	90	90	90	302.46(-30%)

Table 2: Calculated values of lattice constant (c_{ij}) for Y_2S_3, Y_2TeS_2 compound with PBEsol

	C_{11}	C_{12}	C_{13}	C_{22}	C_{23}	C_{33}	C_{44}	C_{55}	C_{66}
Y_2S_3	170.91	57.89	50.52	148.37	68.42	167.13	61.40	65.69	53.79
Y_2TeS_2	117.24	21.24	61.78	150.98	16.84	102.26	25.90	17.48	63.78

such as bonding nature, anisotropy, ductility, hardness, and brittleness. They describe important applications of materials, such as the thermo-physical properties. Elastic constants play a vital role in determining material stability via the Born-Huang criteria (38). For orthorhombic material to achieve mechanical stability, it must satisfy six Born-Huang criteria stated by (39) Equation 3.1:

$$\begin{aligned} C_{11}>0, C_{44}>0, C_{55}>0, C_{66}>0 \\ C_{11}C_{22}>C_{12}^2, \\ C_{11}C_{23}^2C_{33}+2C_{12}C_{13}C_{23} \\ -C11C_{23}^2-C_{22}C_{13}^2-C_{33}C_{12}^2>0 \end{aligned} \tag{3.1}$$

The computed elastic constants (c_{ij}), bulk (B), Young (y), Shear (G), linear compressivility and Poisson's ratio (ν), and energy of cohesion (E_{coh}) for Y_2S_3 and Y_2TeS_2 are listed in Table 2. Having satisfied the criteria stated in Equation 3.1, both materials are mechanically stable. In contrast, materials with larger lattice constants (c_{ij}) and bulk moduli (B_0) are more resistant to compression than those with smaller (c_{ij}) and (B_0). The change of values recorded for c_{11}, c_{33}, and c_{44}, which values are directly related to lattice parameters a, b, and c, and its derived properties the bulk, Young, and shear modulus. The calculated values for Y_2TeS_2 recorded low values as seen in Table 2 and 3 as compared to that of Y_2S_3 signify the crystal structure properties transformation. The Y_2TeS_2 compound is a softer and more flexible material with the incorporation of a Te atom in comparison to the Y_2S_3 structure.

The Poisson ratio describes the material nature of bonding characteristics, and material compressibility is related to shear modulus and Poisson's ratio. The ductility and brittleness of materials are distinguished based on Poisson's ratio, the material with a lower Poisson ratio exhibited a covalent nature of bonding because the directional nature of covalent bonding can limit lateral deformation. The Computed Poisson's ratio for Y_2S_3 and Y_2TeS_2, 0.24 and 0.25 respectively are seen in Table 3. The obtained values are lower suggesting that Y_2S_3 and Y_2TeS_2 are brittle materials, compressible, and can possess covalent or ionic bonding characteristics (40). Cohesive energy (E_{coh}) is the energy required for a free atom and is crucial to material stability and fundamental properties such as thermo-physical and physicochemical properties. Negative cohesive energy confirmed that the materials are energetically stable; the higher the cohesive energy, the greater the stability (41), and Y_2TeS_2 is predicted to be more energetically stable material than the Y_2S_3 seen from the calculated cohesive energy in Table 3.

Table 3: Calculated values Bulk (B), Young (Y) and Shear (G) moduli in GPa, Linear compressibility (β) TP^{-1}, poissons ratio (ν) and energy of cohension (E_{coh}) (eV/atom) for Y_2S_3, Y_2TeS_2 with PBEsol

	B	Y	G	β	ν	E_{coh}
Y_2S_3	93.34	141.70	56.82	3.80	0.25	-6.04
Y_2TeS_2	63.36	98.06	39.42	6.36	0.24	-2.12

Dynamic stability

The thermodynamic behavior of materials is characterized by the phonon dispersion, hence calculating phonon dispersion and density of states is essential for understanding the dynamic stability of Y_2S_3 and the predicted material Yttrium sulphide telluride Y_2TeS_2. The calculated phonon dispersion and projected density of state (PDOs) along high symmetry k-point directions in the Brillouin zone for Y_2S_3 and Y_2TeS_2 are presented in Figures 2 and 3. The primitive unit cell of Y_2S_3 contains twenty atoms, giving rise to sixty phonon modes for a given wave vector ($\omega_{\mathbf{qk}}$), consisting of three acoustic modes and fifty-seven optical mode types. Similarly, the Y_2TeS_2 unit cell contains five atoms, which give rise to fifteen phonon modes of three acoustic and twelve optical modes of ($\omega_{\mathbf{qk}}$).

Analysis of the phonon dispersion and PDOS reveals that there are no negative frequencies observed, as evidenced by Figures 2 and 3. This demonstrates that the investigated Y_2S_3 and Y_2TeS_2 are dynamically stable. There is no available literature to compare results for Y_2TeS_2 calculated lattice dynamic properties, calculation conducted by (19) confirm our dynamic stability calculation for Y_2S_3. The analysis of phonon dispersion from the left panel of Figures 2 and 3, at Γ points reveals that longitudinal acoustic (LA) and transverse acoustic (TA) modes are linear, as seen from Figure 2 for Y_2S_3, while a combination of linear and flat (TA) and (LA) modes is seen from Figure 3 for Y_2TeS_2. The flat acoustic mode is referred to as acoustic attenuation due to the thermoelastic phenomenon or phonon-phonon interaction and localization of state (42). From Figure 2 there is no gap observed in the phonon dispersion between the acoustic and optical modes. Besides in Figure 3, there is a clear band gap separating the acoustic and optical modes in phonon dispersion for the Y_2TeS_2 compound. The presence of a band gap indicated the localization of a state corresponding to the Te-atom peaks in PDOs, which is merely reflected due to the concentration of substitution of tellurium (Te) atoms in the Y_2S_3 structure and the effect of the large mass difference between tellurium (Te) and sulfur (S) and yttrium (Y) atoms and confirmed the structural transformation.

The projected density of states is depicted in the right panel of Figures 2 and 3. The phonon dispersion spectra of solids are known to be influenced by the atomic mass and bonding strength of the constituent atoms. The Y_2TeS_2 phonon dispersion and PDOs are characterized by two parts, the lower frequency region from 0 - 6 THz of acoustic mode and the 6 - 10 THz higher frequency region of optical mode separated by a band gap as depicted in Figure 3. From Figure 3, the phonon spectra for Y_2TeS_2, the acoustic mode of the lower frequency region is dominated by the vibration of the tellurium Te atom, and at high frequency, the optical mode vibration of yttrium, tellurium, and sulfur atoms. It is observed from Figure 2 that the phonon dispersion and PDOs spectra are continuous along acoustic and optical modes for Y_2S_3; therefore, both the lower and higher frequency regions of acoustic and optical modes are dominated by the vibration of yttrium and sulfur atoms.

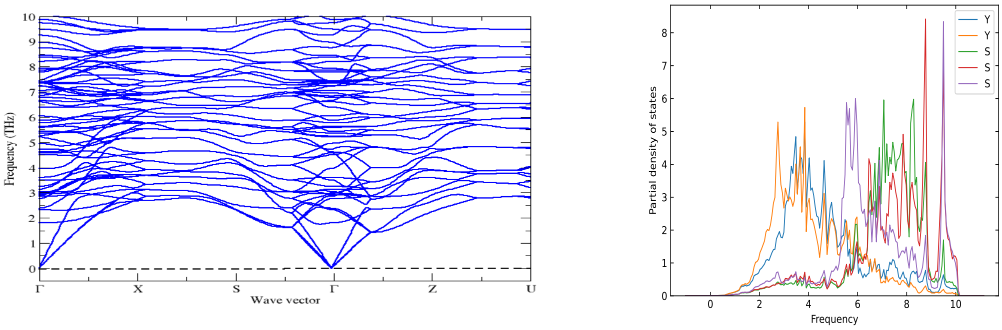

Figure 2: Phonon band structure left and projected density of state calculated with PBEsol for Y_2S_3 compound

Structural stability including mechanical, dynamical, and cohesive energy screening is part of the criteria and requirements for predicting the material possibility of being synthesized. The predicted Y_2TeS_2 from material project database (23), calculated elastic constant results seen in Table 2, the phonon dispersion and cohesive energy seen in Table 3 reveals that Y_2TeS_2 is stable and can be synthesized. The Y_2S_3 material was synthesized, and PBEsol calculation reveals the Y_2S_3 is a stable material for other applications.

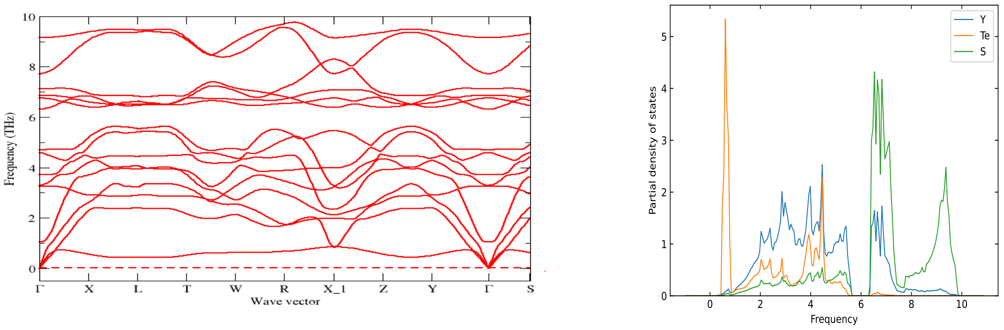

Figure 3: Phonon band structure left and projected density of state calculated with PBEsol for Y_2TeS_3 compound

4 Electronic properties

We study the electronic properties of yttrium sulphide Y_2S_3 and yttrium sulphide telluride Y_2TeS_2 materials. Band structure calculations were performed with the PBEsol functional; the result shows that both materials are semiconductors. The band gap of Y_2S_3 was reported by (19) as pressure-dependent; the band gap decreases with an increase in pressure. The PBE method of calculating band structure is well known for underestimating semiconductor material band gaps by about 40% (43). More accurate methods, such as MJB and HSE06, were employed for better estimation of electronic band gaps. The HSE06 on average was reported as the most reliable method of predicting the material semiconductor electronic properties. The calculated band structure using the PBEsol and MBJ for Y_2S_3 and Y_2TeS_2 are depicted in Figures 4 and 5 and Y_2TeS_2 in Figure 6 and 7 respectively. From Figures 4 and 5 left panel band structure, Y_2S_3 is a semiconductor with a direct band gap at the Γ-point, both the band structure pattern is similar. The band structure left panel Figure 6 and 7 for Y_2TeS_2 reveals that it is a semiconductor with indirect band gap at the Γ and S-points of the wave vector. The right panel of Figures 4 and 5 represents the projected density of state (PDOs) calculated with PBEsol and MBJ has a similar pattern. Conduction band minimum (CBM) and valence band maximum (VBM) of Y_2S_3 are mainly the contribution of Y(d) and S(p), respectively. Figure 6 and 7 shows calculated PDOs using PBEsol and MBJ, CBM, and VBM of Y_2TeS_2 are dominated by Y(d) and Te(p) contribution. Analysis of both materials' PDOs confirmed rare earth element outer valence electron $4d^1$ contribution dominated the CBM and chalcogenide out valence electron S(p) and Te(p) controlled the VBM. The values of band gaps obtained from PBEsol, MBJ, and HSE06 are listed in Table 4. Calculated band gaps for Y_2S_3 are comparable to experimentally measured 2.8 eV (21).

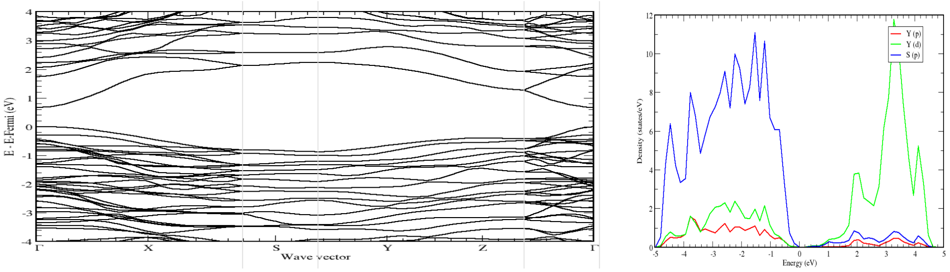

Figure 4: PBEsol calculated band structure left and right projected density of state (PDUs) for Y_2S_3 material.

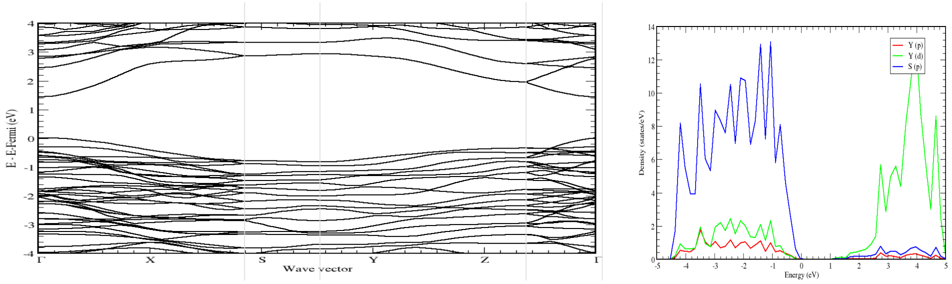

Figure 5: MBJ calculated band structure left and right projected density of state (PDOs) for Y_2S_3 material.

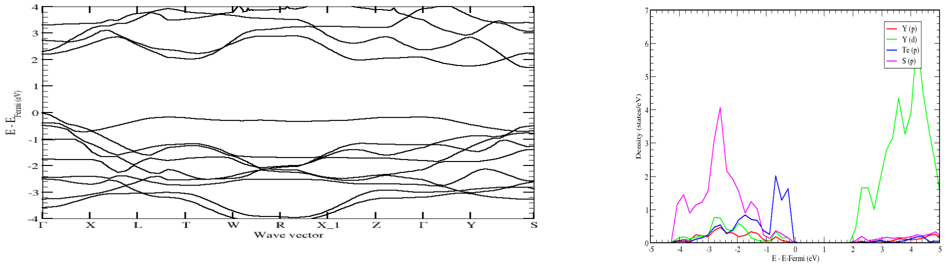

Figure 6: PBEsol calculated band structure left and right projected density of state (PDOs) for Y_2TeS_2 material.

5 Band edge position

Mullikan's electronegativity screening method for band alignment was employed for the energy assessment of the conduction band minimum CBM and valence band maximum VBM potential for bulk semiconductors. In this method, the flat band potential is the electrode potential at which the semiconductor bands are flat (zero space charge) and is measured with reference to the redox potential of normal hydrogen electrode (NHE) at pH = 0. The band edges are predicted and compared to electrode potentials for the normal hydrogen electrode (NHE) scale theoretically using the Butler and Ginley given relation (44; 45; 46):

$$E_{VBM} = \chi - E_e + \frac{1}{2}E_g \tag{5.1}$$

$$E_{CBM} = E_{VBM} - E_g \tag{5.2}$$

where E_{VBM} and E_{CBM} are valence and conduction band edges, χ is the Mulliken electronegativity, E_e is the energy of free electron hydrogen scale (4.5 eV) (45), and E_g is the band gap. For the bulk semiconductor compound, Mulleken electronegativity (χ) in Equation 5.1 is the geometric mean of electronegativities for constituent atoms (47).

$$\chi = (\chi_1^n \chi_2^s .... \chi_{n-1}^p \chi_n^q)^{\frac{1}{N}} \tag{5.3}$$

where χ_n, n, and N are the electronegativity of constituent atoms, the number of species, and the total number of atoms in the compound, respectively.

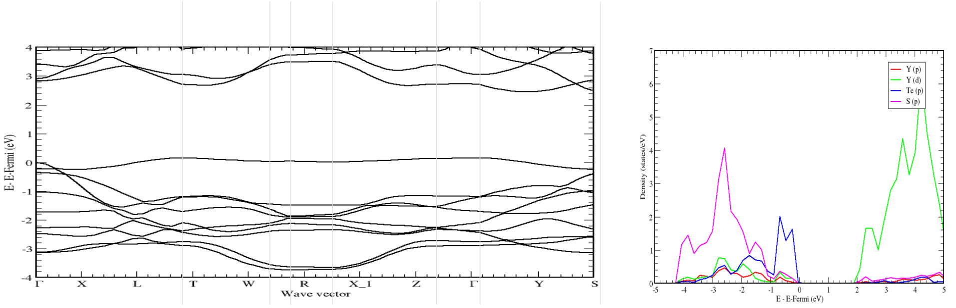

Figure 7: MBJ calculated band structure left and right projected density of state (PDOs) for Y_2TeS_2 material.

Table 4: Calculated band gap (E_g), conduction band minimum (C_{CBM}) and valence band maximum potentials (V_{VBM}) for Y_2S_3 and Y_2TeS_2 compounds

	Y_2S_3				Y_2TeS_2			
	PBEsol	MBJ	HSE06	Exp.	PBEsol	MBJ	HSE06	
E_g (eV)	0.66	1.42	2.75	2.80(21),1.35(19)	1.70	2.30	2.70	
$C_{(CBM)}$			-1.05				-1.30	
$V_{(VBM)}$			1.70				1.4	
Electronegativity (χ)				4.76				4.60

Mullikan's electronegativity screening criteria require that the energy of E_{VBM} is $>$ 1.23 eV and the energy of E_{CBM} is $<$ zero compared to the standard hydrogen electrode (NHE) for reduction H^+/H_2 and oxidation O_2/H_2O reactions, respectively (44). The approach compares the NHE as the band gap energy (E_g) difference between CBM and VBM, which may be $>$ 1.23 eV, which is sufficient for potentials to provide the driving force for crossing the barrier. The positions of (E_{CBM}) and (E_{VBM}) aligned to water oxidation/reduction potential access the ability of redox potential and light absorption for semiconductor materials.According to Eqs. (5.1) and (5.2), the calculation for Y_2S_4; χ = 4.76 HSE band gap 2.75 eV yield E_{VBM} and E_{CBM} values of 1.70 V and -1.05 V, E_{VBM} is 0.47 V higher than the oxidation potential and E_{CBM} is -1.05 V lower than reduction potential compared to NHE electrode. The Y_2TeS_2 with calculated HSE band gap 2.70 eV, χ = 4.60, yields E_{VBM} and E_{CBM} values of 1.40 V and -1.30 V, respectively. E_{VBM} is 0.17 V higher than the oxidation potential, and E_{CBM} is -1.30 V lower than the reduction potential compared to the NHE electrode. It is seen from Figure 8 that all the materials under screening have suitable conduction and valence band edges to trigger the oxygen evolution reaction (OER) and hydrogen evolution reaction (HER) simultaneously.

However, a semiconductor material must possess perfect band edge positions to be thermodynamically stable for water-splitting applications. The band edge positions of VBM and CBM located closer to the redox potentials possess the higher efficiency for photocatalytic water-splitting full reactions (48). Accordingly, both Y_2S_3 and Y_2TeS_2 have suitable VBM band edge positions for oxidation evolution reaction (OER). The calculated values -1.05 V and -1.30 V of conduction band minimum potential (CBM) for Y_2S_3 and Y_2TeS_2 respectively, compared to the normal hydrogen electrode (NHE) are more negative and much lower than the reduction potential seen in 8. This implies overpotential reference to hydrogen reduction potential due to Y_2S_3 and Y_2TeS_2 calculated band gap values of 2.75 eV and 2.70 eV respectively with light absorption efficiency in the ultraviolet (UV) region. The calculated band edge position of Y_2S_3 and Y_2TeS_2 listed in Table 4 are comparable to graphite-like carbon nitrate ($g-C_3N_4$) semiconductor (49). Semiconductor materials with band gaps between 1.6 and 2.3 eV were reported to absorb light in the visible region and have maximum absorption light efficiency for efficient photocatalyst material (50; 51). Although the band edge potential is pH-dependent (51) for bulk semiconductors, our calculations are based on pH = 0; further screening with pH greater than zero will give more understanding of the water-splitting application of Y_2S_3 and Y_2TeS_2 compounds.

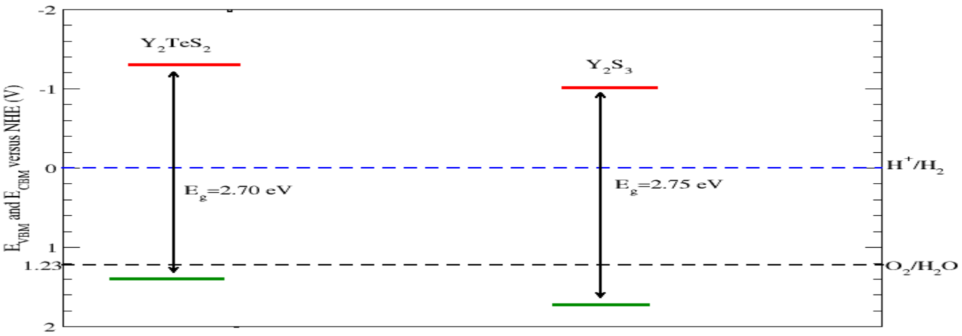

Figure 8: Computated conduction band minimum (CBM) and valence band maximum (VBM) pH = 0, band gap versus normal hydrogen electrode (NHE) for Y_2S_3 and Y_2TeS_2 material.

6 Conclusion

Structural stability; mechanical and dynamic, electronic and photocatalytic properties of Y_2S_3 and Y_2TeS_2 were investigated by the state of art density functional theory. The calculated structural properties revealed that both the materials under screening were orthorhombic crystals, based on the calculated elastic constant and elastic tensor analysis (Elate) derived mechanical properties revealed that Y_2S_3 and Y_2TeS_2 are mechanically stable and the energy of cohesion -2.12 eV/atom reveals that our predicted material Y_2TeS_2 can be synthesized. The phonon dispersion based on finite displacement technique yielded vibrational frequency with no negative frequencies across the wave vector indicating that Y_2S_3 and Y_2TeS_2 are dynamically stable. The electronic properties; band structure and partial density of state calculated from PBEsol, MBJ, and HSE06 revealed that Y_2S_3 and Y_2TeS_2 are wide band gap semiconductors, from HSE06 band gap 2.75 eV and 2.70 eV respectively. The band gap positions can absorbed within the ultra-violet (UV) wavelength. According to PBEsol and MBJ band structures, Y_2S_3 is a direct band gap and Y_2TeS_2 is an indirect band gap semicondutors. We screen Y_2S_3 and Y_2TeS_2 materials for photo-conversion application, and band-edge positions criteria were used to predict water splitting application. Mullikan's electronegativity screen technique based on calculated VBM and CBM band edge potentials predicted that Y_2S_3 and Y_2TeS_2 have suitable conduction and valence band edges to trigger the oxygen evolution reaction (OER) and hydrogen evolution reaction (HER) simultaneously.

7 Acknowledgement

We acknowledge the effort of TETfund-Nigeria for providing the research grant under the institutional-based research funds (IBR) at Jigawa State Polytechnic, Dutse. We also acknowledge the Centre for High Performance Computing (CHPC), South Africa, for providing computational resources to this research project.

References

[1] Wang, X., Tang, Y., Lee, J.M., Fu,. Recent advances in rare-earth-based materials for electrocatalysis. *Chem Catalysis* 2 967 2022.

[2] Gaggero, E., Calza, P., Cerrato, E., et. al., Cerium, europium-and erbium-modified zno and zro2 for photocatalytic water treatment applications. A review. *Catalysts* 11 1520 2021.

---

[3] Habib, I., Zain, N.M., Lim, C.M., Usman, A., Kumara, N., Mahadi, A.H. Effect of doping rare-earth element on the structural, morphological, optical and photocatalytic properties of zno nanoparticles in the degradation of methylene blue dye, IOP Conference Series: *Materials Science* 2004 2021.

[4] Apostolova, I., Apostolov, A., Wesselinowa, J. Band gap tuning in transition metal and rare-earth-ion-doped tio2, ceo2, and sno2 nanoparticles. *Nanomaterials* 13 145 2022.

[5] Kubiak, A., Cegaowski, M., Unraveling the impact of microwave-assisted techniques in the fabrication of yttrium- doped tio2 photocatalyst. *Scientific Reports* 14 262 2024.

[6] Narewadikar, N., Pedanekar, R., Parale, V., Park, et al., Spray deposited yttrium incorporated tio2 photoelectrode for efficient photoelectrocatalytic degradation of organic pollutants. *Journal of Rare Earths* 41 1929–1937 2023.

[7] Ramu, S., Puneetha, P., Reddy, M.S.P., et al., Improved hydrogen evolution and interesting luminescence properties of rare earth ion-doped zns nanoparticles. *Applied Physics A* 129 106 2023.

[8] Chandekar, K.V., Alshahrani, T., Ben Gouider Trabelsi, A., et al., Novel rare earth yttrium doping effect on physical properties of pbs nanostructures facile synthesis and characterization. *Journal of Materials Science* 56 4763–4781 2021.

[9] Ech-Chergui, A.N., Bennabi, F., Isik, M., et al., Bifunctional praseodymium-doped sns2 thin films for photocatalytic and antibacterial applications. Colloids and Surfaces A: Physicochemical and Engineering Aspects 686 133362 2024.

[10] Guo, S.P., Guo, G.C., Crystal structure and magnetic and photocatalytic properties of a new ternary rare-earth mixed chalcogenide, dy 4 s 4 te 3. *Journal of Materials Chemistry A* 2 20621–20628 2014.

[11] Chi, Y., Rong, L.Z., Suen, N.T., et al., Crystal chemistry and photocatalytic properties of re4s4te3(re= gd, ho, er, tm): experimental and theoretical investigations. *Inorganic Chemistry* 57 5343–5351 2018.

[12] Kumari, C., Sharma, P., Katyal, S., et al., Photocatalytic activity of gesbseer quaternary chalcogenide for efficient methylene blue degradation in visible light. *Results in Surfaces and Interfaces* 9 100088 2022.

[13] Guo, S.P., Chi, Y., Zou, J.P., Xue, H.G., Crystal and electronic structures, and photoluminescence and photocatalytic properties of -euzrs3. *New Journal of Chemistry* 40 10219–10226 2016.

[14] Barde, A., Alhassan, U., Computational study of the structural, electronic and optical properties of cubic phase y2mgx4 (x = s, se and te) metal chalcogenide compounds. *International journal research and technopreneurial innovations* 1 129–138 2024.

[15] Seddik, T., Khenata, R., Bouhemadou, A., et al., Prediction study of the structural, elastic and high pressure properties of yttrium chalcogenide. *Computational materials science* 49 372–377 2010.

[16] Wood, C., Lockwood, A., Parker, J., et al., Thermoelectric properties of lanthanum sulphide. *Journal of applied physics* 58 1542–1547 1985.

[17] Gruber, J., Zandi, B., Justice, B., Westrum Jr, E., Optical spectra and thermal schottky levels in the high temperature -phase of the lanthanide sesquisulphides. *Journal of Physics and Chemistry of Solids* 61 1189–1197 2000.

[18] Patil, S.J., Lokhande, C.D., Fabrication and performance evaluation of rare earth lanthanum sulphide film for supercapacitor application: effect of air annealing. *Materials and Design* 87 939–948 2015.

[19] Shen, Z., Wang, L., Yue, L., et al., Irreversible semiconductor-to-semiconductor transition and highly enhanced photoconductivity of y2s3 induced by structural modulation. *Applied Materials Today* 35 102008 2023.

[20] Michiels, J., Gschneidner Jr, K., Electrical properties of yttrium sesquisulphide (y2s3) mechanically alloyed with copper, boron, and aluminum. *Journal of alloys and compounds* 247 9–14 1997.

[21] Nakamura, H., Ogawa, Y., et al., P-type and n-type semiconductivities of solid yttrium sulphide. *Transactions of the Japan institute of metals* 25 698–702 1984.

[22] Range, K.J., Leeb, R., Hochdruckmodifikationender lanthaniden (iii) sulphide ln2s3 (ln= lu-ho, y) mit u2s3-struktur/high pressure modifications of the rare earth sulphides ln2s3 (ln= lu-ho, y) with u2s3-structure. *Zeitschrift für Naturforschung B* 30 889–895 1975.

[23] Jain, A., Ong, S.P., Hautier, G., et al., The Materials Project: A materials genome approach to accelerating materials innovation. *APL Materials* 1 011002 2013.

[24] Kumar, P., Naumov, I.I., Manchanda, P., Dev, P., A new class of intrinsic magnet: two-dimensional yttrium sulphur selenide. *arXiv preprint arXiv.2009.07232* 2020.

[25] Kohn, W., Sham, L.J., Self-consistent equations including exchange and correlation effects. *Physical review* 140 A1133 1965.

[26] Hohenberg, P., Kohn, W., Inhomogeneous electron gas. *Physical review* 136 B864 1964.

[27] Kresse, G., Furthmüller, J., Efficient iterative schemes for ab initio total-energy calculations using a plane-wave basis set. *Physical review B* 54 11169 1996.

[28] Perdew, J.P., Ruzsinszky, A., Csonka, G.I., et al., Restoring the density-gradient expansion for exchange in solids and surfaces. *Physical review letters* 100 136406 2008.

[29] Kresse, G., Joubert, D., From ultrasoft pseudopotentials to the projector augmented-wave method. *Physical review b* 59 1758 1999.

[30] Monkhorst, H.J., Pack, J.D., Special points for brillouin-zone integrations. *Physical review B* 13 5188 1976.

[31] Togo, A., Tanaka, I., First principles phonon calculations in materials science. *Scripta Materialia* 108 1–5 2015.

[32] Alfè, D., Phon: A program to calculate phonons using the small displacement method. *Computer Physics Communications* 180 2622–2633 2009.

[33] Togo, A., First-principles phonon calculations with phonopy and phono3py. *Journal of the Physical Society of Japan* 92 012001 2023.

[34] Tran, F., Blaha, P., Accurate band gaps of semiconductors and insulators with a semilocal exchange-correlation potential. *Physical review letters* 102 226401 2009.

[35] Heyd, J., Scuseria, G.E., Ernzerhof, M., Hybrid functionals based on a screened coulomb potential. *The Journal of chemical physics* 118 8207–8215 2003.

[36] Hassanien, A. S and Akl, A. A., Effect of Se addition on optical and electrical properties of chalcogenide CdSSe thin films. Superlattices and Microstructures, 89, 153-169 2016.

[37] Yu, L., Yan, Q and Ruzsinszky, A., Negative Poisson's ratio in 1T-type crystalline two-dimensional transition metal dichalcogenides. Nature communications, 8(1), 1-8 2017.

[38] Born, M., Huang, K., Dynamical theory of crystal lattices. Oxford university press 1996.

[39] Mouhat, F., Coudert, F.X., Necessary and sufficient elastic stability conditions in various crystal systems. *Physical review B* 90 224104 2014.

[40] Greaves, G. N., Greer, A. L., Lakes, R. S., et al., Poisson's ratio and modern materials. Nature materials, 10(11), 823-837 2011.

[41] Vig, A., Doan, E., Yang, K., First-principles investigation of size effects on cohesive energies of transition-metal nanoclusters. *Nanomaterials* 13 2356 2023.

[42] Singh, D., Behaviour of acoustic attenuation in rare-earth chalcogenides. Materials Chemistry and physics 115 65–68 2009.

[43] Perdew, J.P., Levy, M., Physical content of the exact kohn-sham orbital energies: band gaps and derivative discontinuities. *Physical Review Letters* 51 1884 1983.

---

[44] Butler, M., Ginley, D., Prediction of Flatband potentials at semiconductor-electrolyte interfaces from atomic electronegativities. *Journal of the Electrochemical Society* 125 228 1978.

[45] Morrison, S.R., Morrison, S., Electrochemistry at semiconductor and oxidized metal electrodes. volume (126) Springer 1980.

[46] Nethercot Jr, A.H., Prediction of fermi energies and photoelectric thresholds based on electronegativity concepts. *Physical Review Letters* 33 1088 1974.

[47] Lu, J., Jin, H., Dai, Y., et al., Effect of electronegativity and charge balance on the visible light responsive photocatalytic activity of nonmetal doped anatase tio2. *International Journal of Photoenergy* 928503 2012.

[48] Hu, W., Lin, L., Zhang, R., Yang, C., Yang, J., Highly efficient photocatalytic water splitting over-edge modified phosphorene nanoribbons. *Journal of the American Chemical Society* 139 15429–15436 2017.

[49] Wen, J., Xie, J., Chen, X., Li, X., A review on g-c3n4-based photocatalysts. *Applied surface science* 391 72–123 2017.

[50] Eidsvåg, H., Bentouba, S., Vajeeston, P., et al., Tio2 as a photocatalyst for water splitting experimental and theoretical review. *Molecules* 26 1687 2021.

[51] Yasuda, T., Kato, M., Ichimura, M., Hatayama, T., Sic photoelectrodes for a self-driven water-splitting cell. *Applied Physics Letters* 101 2012.